Title
Experimental investigation of optical breakdown using nanosecond 532-nm and 1064-nm laser pulses delivered at high numerical aperture

Authors
Guerra III, Arnold
Venugopalan, Vasan
Nahen, Kester
et al.

Publication Date
2001-05-10

DOI
10.1117/12.426778

EXPERIMENTAL INVESTIGATION OF OPTICAL BREAKDOWN USING NANOSECOND 532- AND 1064-NM LASER PULSES DELIVERED AT HIGH NUMERICAL APERTURE

Arnold Guerra III[*†], Vasan Venugopalan[*†], Kester Nahen[⋆], and Alfred Vogel[⋆]

[*]Department of Chemical and Biochemical Engineering and Materials Science
University of California, Irvine, CA 92697-2575,

[†]Laser Microbeam and Medical Program, Beckman Laser Institute and Medical Clinic
University of California, Irvine, CA 92612-3010,

and

[⋆]Medical Laser Center, Lübeck, Peter Monnik Weg 4, D-23562, Lübeck GERMANY

Abstract

We have conducted time-resolved studies of optical breakdown produced by the irradiation of water using 6 ns Nd:YAG laser pulses of 1064 nm and 532 nm wavelength focused at a numerical aperture of $NA = 0.9$. We determined pulse energy threshold values for plasma formation to be 1.89 μJ and 18.3 μJ for 532 and 1064 nm irradiation, respectively. These energy thresholds correspond to irradiance thresholds of 0.77×10^9 W / mm^2 for 532 nm irradiation and 1.87×10^9 W / mm^2 for 1064 nm irradiation. For pulse energies 1×, 2×, 5×, and 10× above threshold, we determined the length of the laser-induced plasma, the propagation speed and peak pressures of the emitted shock wave, and the mechanical energy dissipated by subsequent cavitation bubble formation, growth, and collapse. This analysis demonstrates that both the breakdown threshold as well as the conversion efficiency of the incident laser energy into mechanical energy is smaller for irradiation at 532 nm than for 1064 nm. These results are consistent with laser parameters employed for a variety of nanosecond pulsed microirradiation procedures using 1064 nm and 532 nm radiation focused by microscope objectives with large numerical apertures ($NA \gtrsim 0.8$). These results suggest that laser-induced breakdown is the primary mechanism that drives a variety of cellular micromanipulation techniques which employ nanosecond visible and near-infrared laser pulses.

1 Introduction

Laser-induced plasma formation, also known as optical breakdown, is a nonlinear absorption process that occurs when a laser pulse of sufficiently high power is focused into a small volume of a medium. The focused radiation generates a hot plasma (quasifree electrons in the conduction band with density $> 10^{15}$ / mm^3) in the focal volume of the medium through multiphoton and / or cascade ionization via inverse bremsstrahlung absorption. The rapid increase in plasma temperature leads to its explosive expansion resulting in the radiation of a shock wave and in cavitation bubble formation at the emission center.

The formation of plasmas in biological media using nanosecond laser pulses has been the subject of detailed study as it is utilized in such clinical procedures as intraocular microsurgery and laser lithotripsy [5, 10]. In the case of intraocular surgery, pulse energies of 0.1–10 mJ are employed with small laser spot diameters and result in irradiances that typically exceed 10^8 W / mm^2 [10]. In such applications, tissue modification occurs on a spatial scale on the order of 100 μm [12]. Upon examination of the laser parameters used for a variety of pulsed laser microirradiation applications, irradiances on the order of 10^8 W / mm^2

Optical Diagnostics of Living Cells IV, edited by Daniel L. Farkas, Robert C. Leif, Proceedings of SPIE Vol. 4260 (SPIE, Bellingham, WA, 2004) · 0277-786X/04/$15 · doi: 10.1117/12.426778

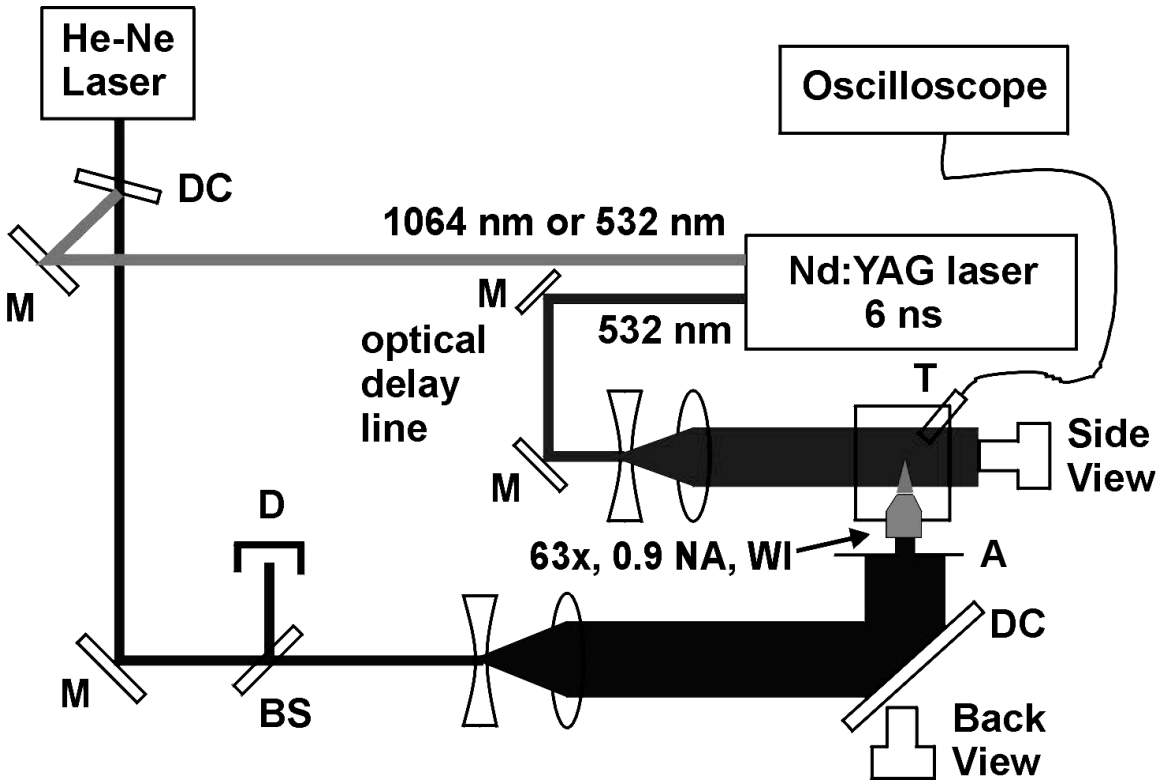

Figure 1: Experimental setup used for time-resolved examination of the dynamics involved in laser-induced breakdown of water. M: mirror, DC: dichroic beam splitter, D: pyroelectric energy detector, T: hydrophone transducer, A: 6 mm aperture.

are routinely employed but result in modification on the micrometer spatial scale or less [1, 2, 7]. The principal difference being that in applications of cell microirradiation, the laser beam is focused to a diffraction limited spot through a cone angle in the range of 70-135° while focusing angles for the clinical applications mentioned above rarely exceed 30°

Thus, to examine the possible role of laser-induced breakdown as a mechanism that drives pulsed laser microirradiation procedures, we have conducted several time-resolved experiments to characterize the dynamics of the optical breakdown process including the resulting shock wave propagation and cavitation bubble formation using nanosecond pulsed laser irradiation in water ***focused at high numerical aperture***. We used distilled water as our sample for convenience as it has been shown that optical breakdown in water is very similar to that in ocular and other biological media [4]. If optical breakdown is indeed found to be the principal mechanism driving pulsed laser microirradiation processes, the information learned from these studies can be used to improve and optimize laser parameters chosen for a particular application.

2 Materials and Methods

The basic experimental setup used for these investigations is shown in Figure 1. The 1064 nm or 532 nm output of a 6 ns Nd:YAG laser was aligned collinearly with a HeNe aiming laser beam. This combined beam was expanded using a -40 mm negative lens and recollimated using a 200 mm focal length achromat lens. This expanded beam was reflected off a short pass dichroic beamsplitter thereby directing

the laser beam through a 6-mm diameter aperture to overfill the back aperture of a 63×, 0.9 numerical aperture water immersion microscope objective (Leica). The microscope objective was introduced through a hole machined into the wall of a water filled cuvette to allow irradiation of the water sample without optical aberrations which have been shown to significantly affect the optical breakdown process [13]. To image the plasma and subsequent hydrodynamic events we employed two 35mm cameras using either Kodak TMAX 100 or Agfapan APX 25 photographic film. To provide a 'back view' of the process, one of these cameras was placed behind the dichroic and fitted with a 105 mm lens. This allowed us to visualize the plasma using the inherent magnification of the microscope objective and resulted in a composite magnification of approximately 30×. The second camera was outfitted with a 7× lens (Leitz Photar) to provide a 'side view' of the plasma formation and associated hydrodynamic phenomena. The energy of each laser pulse was monitored by a pyroelectric detector and calibrated to the true energy delivered to the sample.

2.1 Determination of threshold energy for plasma formation

A total of 20 individual laser pulses of fixed energy were delivered to the water-filled cuvette in a dark room. The number of pulses which resulted in plasma formation, as determined by the appearance of a visible flash, was noted. This procedure was repeated for several (15-20) pulse energies to allow for a determination of the variation in the probability of plasma formation with pulse energy. The probability of plasma formation vs. pulse energy was plotted and fitted to a Gaussian error function. The pulse energy at which the probability of plasma formation is 50% was determined and denoted as the energy threshold E_{th} for plasma formation / optical breakdown [14].

2.2 Determination of plasma size

The size of the laser-induced plasmas was determined by examining photographs of the radiant emission at pulse energies 1×, 2×, 5×, and 10× the threshold energy from both back and side views. For these photographs, no external illumination was employed and the camera shutter was manually opened prior to the laser pulse emission and closed promptly thereafter. When photographed from the side view, the plasma image on the film negative was roughly elliptical in shape and examined using a biological dissection microscope (Olympus BH-2) in which we measured both its length (major axis) and the diameter (minor axis). The size of the plasma on the film negative was converted to its true size by accounting for the magnification produced by the camera-lens assembly. This magnification was determined by photographing a US Air Force resolution test slide placed in the focal plane of the objective and comparing the size of the markings on the film negative with their true size.

2.3 Determination of shock wave dynamics

The dynamics of the shock wave propagation was photographed from side view only. To measure the propagation of the shock wave, we photographed the position of the shock wave front at several discrete times after the laser pulse. To do this we transilluminated the volume surrounding the focus using a 6-ns 'probe' pulse of 532 nm radiation supplied from the Nd:YAG laser at a specific time delay relative to the 'pump' pulse that produces the laser-induced plasma. Several specific time delays between the pump and probe pulses were set using an optical delay line as shown in Fig. 1. By opening the camera shutter manually prior to the laser pulse emission and closing it promptly thereafter, the position of the shock wave was recorded photographically at delay times ranging from 0-32 ns relative to the pump laser pulse.

2.4 Determination of cavitation bubble dynamics

The dynamics of the cavitation bubble formed by the expanding plasma was photographed from the side view at specific times during its evolution. Because the dynamics of the bubble growth and collapse

occurs on a timescale of the order of tens of microseconds, the use of an optical delay line becomes impractical. Instead, we employed an ultrashort duration (<20 ns) flashlamp triggered by a timed electronic delay to provide the transillumination of the optical field. In addition, a PVDF needle hydrophone (Ceram) with a rise time of 12 ns and 1 mm^2 active area was placed at a distance of 10 mm directly above the focal volume to measure the acoustic emission produced by the shock wave and subsequent cavitation dynamics.

3 Results and Discussion

In these experiments, the pump laser pulse was focused into a small volume within the water sample using a 63×, water immersion microscope objective with $NA = 0.9$. Because the pump laser beam completely filled the back aperture of the objective and possessed a uniform spatial intensity profile we assume diffraction limited conditions to determine that the focused laser spot diameter, $d = 1.22\lambda/NA$, was 0.72 μm for 532 nm and 1.44μm for 1064 nm irradiation. Similarly, the Rayleigh range, $z_R = \pi d^2/4\lambda$, was determined to be 0.77 μm for 532 nm and 1.54 μm for 1064 nm irradiation. Defining the focal volume of the laser beam in the water as consisting of a cylinder with diameter equal to the focused laser spot diameter and with length equal to twice the Rayleigh range, the focal volume was 0.63 μm^3 for 532 nm, and 5.02 μm^3 for 1064 nm irradiation.

3.1 Energy thresholds for plasma formation

Our determination of the probability of plasma formation at various pulse energies resulted in energy threshold values E_{th} of 1.89 μJ and 18.3 μJ for 532 nm and 1064 nm irradiation, respectively. For the focused laser spot diameters determined above, these threshold energies correspond to threshold irradiances I_{th} of 0.77 ×10^9 W / mm^2 and 1.87 ×10^9 W / mm^2 for 532 nm and 1064 nm irradiation, respectively.

These energy and irradiance thresholds are remarkably similar to the energies and irradiances employed in optoinjection, a pulsed laser microirradiation technique in which an exogenous molecule is delivered to a single cell via the pulsed microirradiation of the plasma cell membrane [7]. When using an oil immersion objective with a numerical aperture of $NA = 1.3$, optoinjection is routinely performed at pulse energies of 0.5 μJ and 12 μJ for 532 and 1064 nm irradiation, respectively. These energy values correspond to irradiances of 0.51 ×10^9 W / mm^2 and 3.1 ×10^9 W / mm^2 for 532 and 1064 nm irradiation, respectively.

3.2 Photographic examination of plasma size

Optical breakdown in water was induced using pump pulse energies E_p of 1×, 2×, 5×, and 10× threshold. The shape of the plasmas generated by 532 nm irradiation was ellipsoidal, appearing elliptical in the side-view photographs and circular in the back-view photographs. The ellipsoidal shape mimics that of the focal volume. This visual pattern held for pulse energies corresponding to 1×, 2×, 5×, and 10× threshold. The plasmas generated using 1064 nm irradiation also appeared ellipsoidal for energies near threshold, but exhibited a 'bow-tie' shape in the side-view at pulse energies corresponding to 5× and 10× threshold.

The plasma length *l*, diameter *d*, and equivalent spherical radius *r* for the various pulse energies and irradiation wavelengths are listed in Table 1. The equivalent spherical radius is defined as the radius of the sphere that possesses a volume equivalent to that of the ellipsoidal plasma. The volume of the plasma generated using the 532 nm laser light, at threshold, was 10.3 μm^3. Thus at 532 nm, the plasma volume is larger than the focal volume of the laser beam by a factor of 16.3.

This enlargement of the plasma relative to the focal volume is mainly a result of the luminescence emitted by the plasma during the plasma expansion. The plasma generated at threshold using 1064 nm

Wavelength λ [nm]	Normalized Pulse Energy $\beta = (E_p/E_{th})$	Plasma Length l [μm]	Plasma Diameter d [μm]	Equivalent Radius r [μm]
1064	1	14.0	8.9	5.2
1064	2	25.0	15.5	9.1
1064	5	37.9	21.0	12.8
1064	10	47.3	27.5	16.5
532	1	3.6	2.3	1.35
532	2	3.8	2.9	1.6
532	5	8.4	5.1	3.0
532	10	12.6	7.6	4.5

Table 1: Listing of plasma dimensions and their variation with pulse energy.

irradiation occupies a volume of 589 μm^3, which is larger than the focal volume of the laser beam by a factor of 117. The even larger difference between the size of the focal and plasma volumes produced by 1064 nm breakdown is mainly due to the high irradiance required to generate the quasifree electrons in the conduction band through multiphoton ionization compared to the irradiance required to complete the cascade ionization process during the laser pulse duration. When the plasma begins to form during the times corresponding to the leading edge of the incident laser pulse, the electron-hole recombination results in the emission of radiation at UV wavelengths. This UV radiation then contributes to the formation of additional quasifree electrons in the vicinity of the plasma that act as seed electrons for cascade ionization. Optical breakdown occurs in all regions of the water sample where the irradiance is large enough to complete the ionization cascade up to a critical electron density. The high irradiance threshold for the generation of quasifree electrons through multiphoton ionization accounts for both the higher pulse energy threshold and larger plasma size at 1064 nm compared to 532 nm.

3.3 Shock wave propagation and cavitation dynamics

Time-resolved photography allows for the determination of the shock wave propagation speed and peak pressure. The radii of the shock waves were measured at various times (up to 32 ns) after the generation of the plasma. The expression

$$r_s(t) = a_0 + a_1 t + a_2 \ln(t) \tag{1}$$

was used to fit the experimental values of the shock wave radii $r_s(t)$ [8]. The parameters a_0 and a_2 were chosen to best fit the experimental data. The parameter a_1 was chosen to be equal to the speed of sound in water, namely $c_0 = 1483$ m/s. Figure 2a shows the measured radii describing the temporal evolution of the shock wave produced by 1064 nm irradiation at 5$\times$ threshold as well as the fitted curve to the experimental data. Differentiation with respect to time of such fitted curves yields the temporal variation of the shock wave propagation speed. Figure 2b displays these curves for 1064 nm irradiation at pulse energies 2$\times$, 5$\times$, and 10$\times$ threshold. In these plots the delay time represents the interval between the arrival of the pump pulse and the illumination probe pulse at the breakdown site. In all cases, the speed decreases monotonically to the sonic speed in water. For any specific time delay, the shock wave speed monotonically decreases with the normalized pump pulse energy β. The initial speed exceeds the sonic speed by a factor of 3.7 for the 10$\times$ threshold condition. However, the speeds reported by Fig. 2b must be interpreted with care because at early times the shock wave has not yet detached from the plasma rim and thus the speed represents that of the plasma expansion and not the shock wave.

Using the equation of state for water, we can relate the shock wave propagation speed u_s to its peak

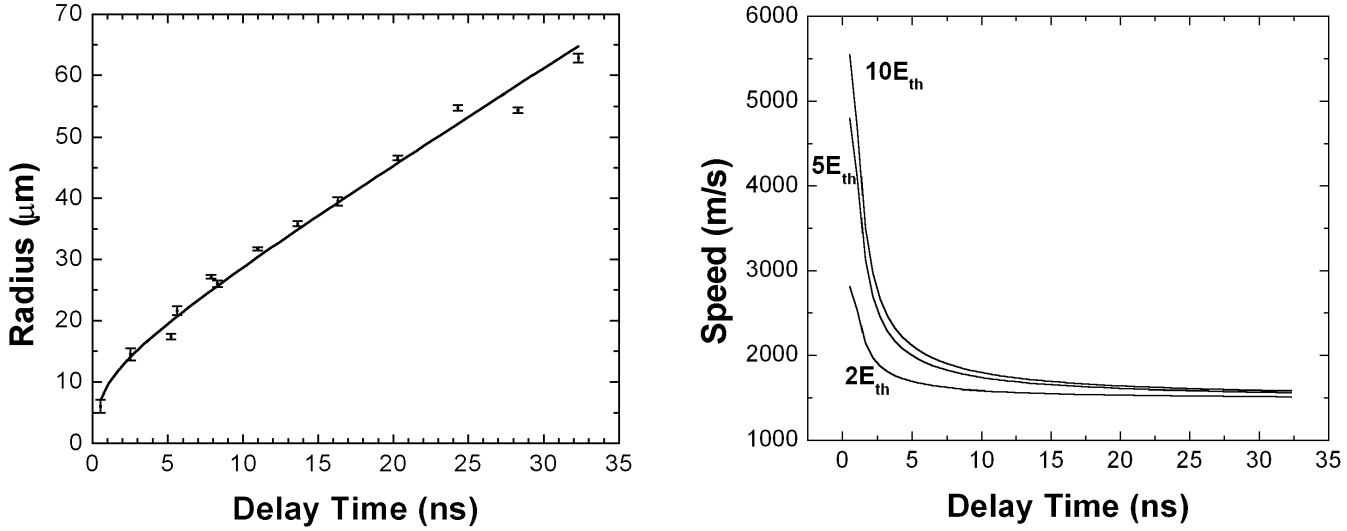

Figure 2: (a) Experimental data for the shock wave radius as a function of time for 1064 nm irradiation at 5× threshold. The curve is the best fit to eq. (1). (b) Derived shock wave velocities as a function of time after Nd:YAG 1064 nm irradiation for pulse energies 2×, 5× and 10× threshold.

pressure p_s [11]

$$p_s = A\rho_0 u_s \left[10^{(u_s - c_0)/B} - 1\right] \tag{2}$$

where $\rho_0 = 998$ kg/m^3 is the mass density of the unperturbed water, $A = 5190$ m/s, and $B = 25306$ m/s. The empirical constants A and B are determined from Rankine-Hugoniot data [9]. In Figure 3 we present the shock wave peak pressure versus propagation distance from the emission center at 1064 nm irradiation for pulse energies of 2×, 5×, and 10× threshold. In this figure we attempted to accurately represent the shock wave pressure by discarding the pressures at distances smaller than the plasma size as reported in Table 1. This effectively excludes the velocity data taken prior to the detachment of the shock wave from the plasma rim.

In Table 2 we list the results of the shock wave pressure measured with the hydrophone at a distance of $r_s = 10$ mm from the focal volume. The energy of a spherical shock wave E_S of radius r_s may be expressed as [15]

$$E_S = \frac{4\pi r_s^2}{\rho_0 c_0} \int p_s^2 \, dt. \tag{3}$$

Assuming the profile of the shock wave is that of an exponential pulse with a full width at half maximum temporal width Δt_S equal to that given by the hydrophone measurements, the energy of the shock wave becomes [15]

$$E_S = 6.124 \times 10^{-9} p_s^2 r_s^2 \Delta t_S \tag{4}$$

where the shock wave energy E_S is in J, shock wave peak pressure p_s is in MPa, the shock wave radius r_s is in m, and Δt_S is in ns. The results of the measurement of the shock wave pressure, shock wave energy E_S, as well as the ratio of the shock wave energy to the laser pump pulse energy (E_S/E_p) at $r_s = 10$ mm from the emission center are listed in Table 2. It is important to note that the shock wave energy calculated at $r_s = 10$ mm from the focal volume represents only about 10-15% of the total shock wave energy

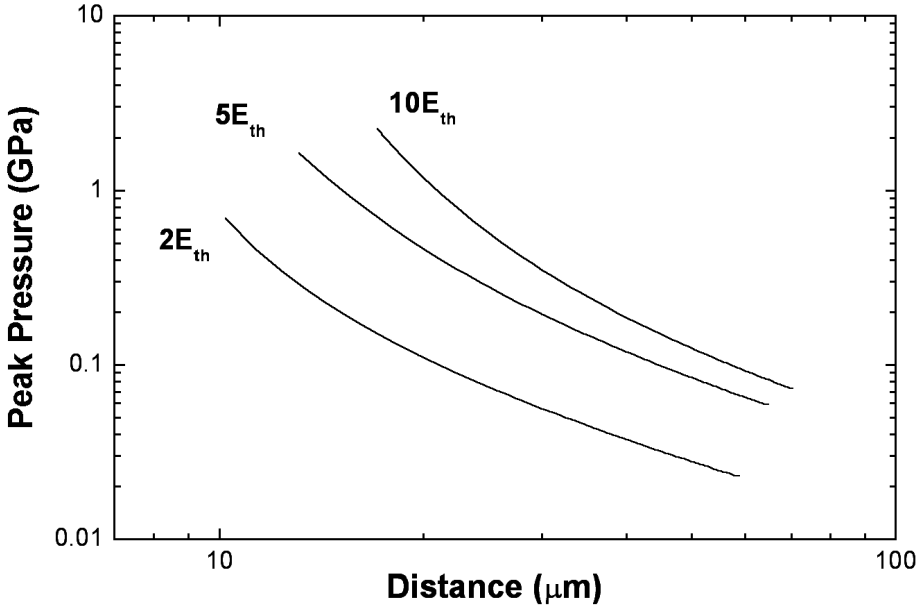

Figure 3: Shock wave pressure vs. propagation distance generated by 1064 nm irradiation for pulse energies 2×, 5×, and 10× threshold.

because most of this energy is dissipated during its propagation in the near field [11, 15]. Nevertheless, the ratio (E_S/E_p) is a measure of the efficiency of conversion of laser light energy into mechanical energy in the water sample and is also indicative of the energy density in the plasma generated in the sample. The results reported in Table 2 demonstrate that when considering equivalent normalized pulse energies β, the conversion of laser light energy into shock wave energy is smaller for 532 nm than for 1064 nm irradiation.

The hydrophone measurements provided values for the cavitation bubble oscillation period T_{osc}, which is related to the maximum cavitation bubble radius R_{max} via the Rayleigh formula [3]. The energy of the spherical cavitation bubble may be expressed as [3, 11]

$$E_B = \frac{4}{3}\pi\rho_0 \left(\frac{2 \times 0.915}{T_{osc}}\right)^2 R_{max}^5. \tag{5}$$

The values of the cavitation bubble energy E_B, and of the ratio of the cavitation bubble energy to the incident laser pulse energy (E_B/E_p), are listed in Table 2. Notice that the conversion efficiency of laser pulse energy into the bubble energy is higher for 1064 nm than for 532 nm and is similar to the result obtained for the shock wave energy.

4 Conclusion

We have examined the dynamics of optical breakdown by performing time-resolved measurements of laser-induced optical breakdown in water using Nd:YAG laser pulses (6 ns, λ=1064 nm and 532 nm) focused using a microscope objective with a numerical aperture of 0.9. We obtain the result that the threshold energy and the conversion of laser pulse energy into mechanical energy is lower for optical breakdown achieved using 532 nm radiation compared to 1064 nm radiation. The pulse energy and irradiance threshold values are similar to those for pulsed laser microsurgery within cells using microscope

λ [nm]	β	E_p [μJ]	Δt_S [ns]	p_s [MPa]	E_S [μJ]	(E_S/E_p) [%]	T_{osc} [μs]	R_{max} [μm]	E_B [μJ]	(E_B/E_p) [%]
1064	1	18.0±0.1	42.0±0.5	0.158±0.028	0.64	3.6	27.7	151.3	1.45	9.1
1064	2	36.4±0.2	47.5±1.0	0.283±0.008	2.33	6.4	45.3	247.6	6.35	17.3
1064	5	90.9±0.3	53.0±0.5	0.475±0.009	7.32	8.1	65.9	360.1	19.57	21.5
1064	10	182.2±0.9	59.0±0.5	0.659±0.005	15.69	8.6	86.6	473.3	44.41	24.4
532	1	1.89±0.10	26.0±0.5	0.038±0.008	0.023	1.2	8.3	45.4	0.039	2.1
532	2	3.78±0.13	31.0±0.5	0.091±0.005	0.157	4.2	13.8	75.4	0.180	4.2
532	5	9.19±0.30	36.0±0.5	0.202±0.008	0.90	9.8	26.9	147.0	1.33	14.3
532	10	19.15±0.60	43.0±0.5	0.310±0.001	2.53	13.2	37.5	205.0	3.60	19.3

Table 2: List of shock wave and cavitation bubble dynamics parameters generated with pump pulse energies of 1×, 2×, 5× and 10× threshold in water for 532 nm and 1064 nm irradiation. The parameters listed are the width of the pressure transient as measured by the hydrophone Δt_S, the pump pulse energy E_p, the shock wave pressure at 10 mm from the optical breakdown site p_s, the shock wave energy at 10 mm from the optical breakdown site E_s, the cavitation bubble oscillation period T_{osc}, the maximum cavitation bubble radius R_{max} and the cavitation bubble energy E_B.

objectives with high numerical aperture. The reduced conversion efficiency of laser pulse energy to shock wave and cavitation bubble energy at pulse energies close to the optical breakdown threshold indicate that the use of 532 nm radiation may offer a means to produce more subtle or precise cellular manipulations that 1064 nm irradiation. This analysis is consistent with the experience in cell microsurgery in which it is much easier to control and produce fine lesions using 532 nm irradiation rather than 1064 nm irradiation [6]. These results strongly suggest that laser-induced breakdown is the primary working mechanism of a variety of pulsed laser microirradiation techniques including cell microsurgery, optoinjection and optoporation.

Acknowledgments: This work was made possible through support from the Laser Microbeam and Medical Program, a NIH Biotechnology Resource (P41-RR-01192), a NIH Bioengineering Research Partnership Award (R01-RR-14892), the Department of Chemical and Biochemical Engineering and Materials Science at the University of California, Irvine, and the German Research Foundation (DFG, grant Bi321/2-4). Experiments were performed at the Medical Laser Center, Lübeck.

References

[1] M. W. Berns, J. Aist, J. Edwards, K. Strahs, J. Girton, P. McNeill, J. B. Rattner, M. Kitzes, M. Hammer-Wilson, L-H. Liaw, A. Siemens, M. Koonce, S. Peterson, S. Brenner, J. Burt, R. Walter, P. J. Bryant, D. van Dyk, J. Coulombe, T. Cahill, and G. S. Berns. Laser microsurgery in cell and developmental biology. *Science*, 213:505–513, 1981.

[2] M. W. Berns, W. H. Wright, and R. W. Steubing. Laser microbeam as a tool in cell biology. *Int. Rev. Cytol.*, 129:1–44, 1991.

[3] C. E. Brennen. *Cavitation and Bubble Dynamics.* Oxford University Press, New York, 1995.

[4] F. Docchio, C. A. Sacchi, and J. Marshall. Experimental investigation of optical breakdown thresholds in ocular media under single pulse irradiation with different pulse durations. *Lasers Ophthalmol.*, 1:83–93, 1986.

[5] S. J. Gitomer and R. D. Jones. Laser-Produced plasmas in medicine. *IEEE Trans. Plasma Sci.*, 19(6):1209–1219, 1991.

[6] T. B. Krasieva. Personal communication, Beckman Laser Institute. 1997.

[7] T. B. Krasieva, C. F. Chapman, V. J. Lamorte, V. Venugopalan, M. W. Berns, and B. J. Tromberg. Cell permeabilization and molecular transport by laser microirradiation. *Proc. Soc. Photo. Instrum. Eng.*, 3260:38–44, 1998.

[8] J. Noack and A. Vogel. Single-shot spatially resolved characterization of laser-induced shock waves in water. *Appl. Opt.*, 37(19):4092–4099, 1998.

[9] M. H. Rice and J. M. Walsh. Equation of state of water to 250 kilobars. *J. Chem. Phys.*, 26(4):824–830, 1957.

[10] A. Vogel. Nonlinear absorption: intaocular microsurgery and laser lithotripsy. *Phys. Med. Biol.*, 42(5):895–912, 1997.

[11] A. Vogel, S. Busch, and U. Parlitz. Shock wave emission and cavitation bubble generation by picosecond and nanosecond optical breakdown in water. *J. Acoust. Soc. Am.*, 100(1):148–165, 1996.

[12] A. Vogel, M. R. C. Capon, M. N. Asiyo-Vogel, and R. Birngruber. Intraocular photodisruption with picosecond and nanosecond laser pulses: Tissue effects in cornea, lens, and retina. *Invest. Ophthalm. Vis. Sci.*, 35(7):3032–3044, 1994.

[13] A. Vogel, K. Nahen, D. Theisen, R. Birngruber, R. J. Thomas, and B. A. Rockwell. Influence of optical aberrations on laser-induced plasma formation in water and their consequences for intraocular photodisruption. *Appl. Optics*, 38(16):3636–3643, 1999.

[14] A. Vogel, K. Nahen, D. Theisen, and J. Noack. Plasma formation in water by picosecond and nanosecond Nd:YAG laser pulses—Part I: Optical breakdown at threshold and superthreshold irradiance. *IEEE J. Sel. Top. Quantum Elec.*, 2(4):847–860, 1996.

[15] A. Vogel, J. Noack, K. Nahen, D. Theisen, S. Busch, U. Parlitz, D. X. Hammer, G. D. Noojin, B. A. Rockwell, and R. Birngruber. Energy balance of optical breakdown in water at nansecond to femtosecond time scales. *Appl. Phys. B*, 68(3):271–280, 1999.